# Ultraviolet A light induces DNA damage and estrogen-DNA adducts in Fuchs endothelial corneal dystrophy causing females to be more affected

Cailing Liu[a,b], Taiga Miyajima[a,b,1], Geetha Melangath[a,b,1], Takashi Miyai[a,b], Shivakumar Vasanth[a,b], Neha Deshpande[a,b], Varun Kumar[a,b], Stephan Ong Tone[a,b], Reena Gupta[a,b], Shan Zhu[a,b], Dijana Vojnovic[a,b], Yuming Chen[a,b], Eleanor G. Rogan[c], Bodhiswatta Mondal[c], Muhammad Zahid[c], and Ula V. Jurkunas[a,b,2]

[a]Schepens Eye Research Institute of Massachusetts Eye and Ear, Boston, MA 02114; [b]Department of Ophthalmology, Harvard Medical School, Boston, MA 02115; and [c]Department of Environmental, Agricultural and Occupational Health, College of Public Health, University of Nebraska Medical Center, Omaha, NE 68198-4388

Edited by Thaddeus Dryja, Harvard Medical School, Boston, MA, and approved November 18, 2019 (received for review July 21, 2019)

**Fuchs endothelial corneal dystrophy (FECD) is a leading cause of corneal endothelial (CE) degeneration resulting in impaired visual acuity. It is a genetically complex and age-related disorder, with higher incidence in females. In this study, we established a nongenetic FECD animal model based on the physiologic outcome of CE susceptibility to oxidative stress by demonstrating that corneal exposure to ultraviolet A (UVA) recapitulates the morphological and molecular changes of FECD. Targeted irradiation of mouse corneas with UVA induced reactive oxygen species (ROS) production in the aqueous humor, and caused greater CE cell loss, including loss of ZO-1 junctional contacts and corneal edema, in female than male mice, characteristic of late-onset FECD. UVA irradiation caused greater mitochondrial DNA (mtDNA) and nuclear DNA (nDNA) damage in female mice, indicative of the sex-driven differential response of the CE to UVA, thus accounting for more severe phenotype in females. The sex-dependent effect of UVA was driven by the activation of estrogen-metabolizing enzyme CYP1B1 and formation of reactive estrogen metabolites and estrogen-DNA adducts in female but not male mice. Supplementation of *N*-acetylcysteine (NAC), a scavenger of reactive oxygen species (ROS), diminished the morphological and molecular changes induced by UVA in vivo. This study investigates the molecular mechanisms of environmental factors in FECD pathogenesis and demonstrates a strong link between UVA-induced estrogen metabolism and increased susceptibility of females for FECD development.**

Fuchs endothelial corneal dystrophy | ultraviolet light | estrogen metabolism | CYP1B1 | mitochondrial DNA damage

The corneal endothelium (CE) is situated in the posterior cornea and serves a key role in maintaining corneal clarity by constant pumping of ions and providing a barrier between the corneal stroma and the aqueous humor. The CE is arrested in the postmitotic state and has limited ability to proliferate in vivo; therefore, loss of cells beyond the threshold functional reserve leads to corneal edema requiring corneal transplantation to restore vision (1–3). Fuchs endothelial corneal dystrophy (FECD), the most common cause of endogenous CE cell loss, is an age-related complex genetic disorder which manifests in the formation of extracellular matrix deposits, known as guttae, and CE cell apoptosis (4). The formation of guttae and CE cell loss starts in the center of the cornea and extends into the periphery as FECD progresses. The cornea is in the direct path of ultraviolet (UV) light, and the central cornea receives a substantially greater penetration of UV light compared to the peripheral regions (5, 6). Specifically, the ultraviolet A (UVA) light (320 to 400 nm) represents 95% of incident solar radiation and is absorbed by all layers of the cornea (epithelium, stroma, and endothelium) (6). Unlike the shorter wavelength UVB (280 to 320 nm) that directly damages the DNA, UVA causes macromolecular toxicity by photoproduction of reactive oxygen species (ROS) (7, 8). Due to high metabolic activity and postmitotic arrest, the CE is especially susceptible to the damaging effects of UV radiation, indicated by the increased accumulation of (nuclear) oxidative DNA damage and premature senescence in the central and not peripheral CE in the "normally" aging corneas (9). Our previous studies have shown that the cornerstone to FECD pathogenesis is the chronic accumulation of DNA damage, both mitochondrial (mtDNA) and nuclear (nDNA), that, in turn, leads to mitochondrial dysfunction and apoptosis in FECD (10). However, the role of UV light in causing DNA damage and endothelial cell degeneration in FECD has not been explored. Specifically, the temporal effect of UV light-induced mtDNA and nDNA oxidative damage on the functioning of postmitotic cells in vivo has not been extensively studied.

One of the key characteristics of FECD is its greater prevalence in females. Late-onset FECD has greater incidence in women, at a ratio of 3- to 4:1 (11, 12). Central corneal guttae have been found in up to 9% (12) to 11% (13) of women while only 3.5% (12) to 7% (13) of men showed similar findings. A higher frequency of more advanced FECD has also been reported in women compared

## Significance

FECD is a genetic and female-predominant disorder which is the leading cause of corneal transplantation worldwide. There are no pharmacologic treatments for FECD; thus, there is a significant unmet need to improve the understanding of female prevalence in FECD pathogenesis. Herein, we reveal a physiologically relevant mechanism of UVA light causing DNA damage and inducing FECD, where greater DNA damage correlates with more severe FECD phenotype in females. Importantly, the sex-dependent effect of UVA is driven by the activation of CYP1B1, an enzyme which converts estrogen into metabolites that cause DNA damage. This study demonstrates an in vivo FECD model based on CE susceptibility to oxidative stress; furthermore, an antioxidant, NAC, restores UVA-induced changes, providing a potential therapeutic target.

Author contributions: C.L., T. Miyajima, G.M., T. Miyai, S.V., N.D., V.K., R.G., S.Z., D.V., Y.C., E.G.R., M.Z., and U.V.J. designed research; C.L., T. Miyajima, G.M., T. Miyai, S.V., N.D., V.K., R.G., S.Z., D.V., Y.C., B.M., and M.Z. performed research; B.M. prepared samples and ran them on an ultraperformance liquid chromatography–tandem mass spectrometer; E.G.R. and M.Z. contributed new reagents/analytic tools; C.L., T. Miyajima, G.M., T. Miyai, S.V., N.D., V.K., S.O.T., R.G., S.Z., D.V., Y.C., E.G.R., M.Z., and U.V.J. analyzed data; and C.L., G.M., S.V., and U.V.J. wrote the paper.

The authors declare no competing interest.

This article is a PNAS Direct Submission.



[1]T. Miyajima and G.M. contributed equally to this work.

[2]To whom correspondence may be addressed. Email: ula_jurkunas@meei.harvard.edu.

This article contains supporting information online at https://www.pnas.org/lookup/suppl/doi:10.1073/pnas.1912546116/-/DCSupplemental.

First published December 18, 2019.

to men (14). Female sex, in addition to age, is the most significant risk factor for advanced FECD development (15). A possible hormonal role has been postulated to account for the increased incidence and more severe phenotypic expression of FECD in females (16); however, no definitive studies have been reported. Impaired endogenous estrogen metabolism has been associated with increased breast cancer risk due to cytochrome P450 (CYP) 1B1 (CYP1B1)-mediated oxidation of estrogens to reactive quinones, which cause DNA damage (17, 18). CYP1B1 is a member of the CYP family and is expressed in adult tissues (19). It catalyzes the 4-hydroxylation of estrone ($E_1$) and estradiol ($E_2$) into catechol estrogens [4-$OHE_1(E_2)$], favoring estrogen quinone [$E_1(E_2)$-3,4-Q] formation. The quinones, in turn, react with DNA and form depurinating DNA adducts and apurinic sites in DNA (see Fig. 4*A*) (17, 18). In addition, there are sex differences in the CYP isoform expression levels, and CYP1B1 is highly expressed in estrogen-related tissues in females (19, 20). For this purpose, we further explored the mechanism of UV-based induction of estrogen metabolism and subsequent DNA damage and how it contributes to the increased incidence and severity of FECD in females.

In this study, we exploited the transparent property of the cornea and created an in vivo model that provides direct visualization of the cellular behavior in response to UV light, as determined by in vivo confocal microscopy and optical coherence tomography (OCT), monitoring the swelling of the cornea as a function of endothelial cell number and morphology. Moreover, we correlated the cellular findings with macromolecular damage (nDNA and mtDNA damage) at different time points of endothelial cell degeneration. Interestingly, our study detected that UVA, the most physiologically relevant light transmitted into the eye (5), leads to phenotypic and molecular changes consistent with FECD. Interestingly, female mice preferentially developed symptoms at low dose UVA, mimicking the status of female human patients, which comprise 75% of the patients undergoing corneal transplantation. We identified the involvement of CYP1B1, the key estrogen-metabolizing enzyme, in sex-dependent differences in CE susceptibility to UVA and detected greater mtDNA damage and estrogen-DNA adduct formation in more severely affected female mice. This study explores the role of UVA in causing DNA damage and activating the estrogen genotoxic pathway in the CE in vivo.

## Results

**UVA Irradiation Causes Progressive Alterations in Mouse Corneal Endothelial Cell Morphology and Greater Cell Loss in Females.** The clinical hallmark of FECD is formation of dome-shaped extracellular matrix deposits called guttae (red arrowheads and white arrows, Fig. 1*A*) and CE cell loss in the central cornea, often sparing in the peripheral cornea or areas covered by eyelids that shield the eye from UV light, as demonstrated by the slit lamp (Fig. 1 *A*, *Middle*) and in vivo confocal (Fig. 1 *A*, *Right*) images of the FECD patient cornea (Fig. 1*A*). This suggests positive correlation of guttae formation and the exposure of UVA in the central cornea. FECD is characterized by a decline in CE cell number and morphological changes manifested by loss of regular hexagonal shape (% hexagonality) and an increase in cell size and shape variability (coefficient of variation). To demonstrate the physiological importance of UVA in FECD pathogenesis, we developed an in vivo UVA-induced late onset FECD mouse model. We established an experimental setup where the right cornea of the mouse eye (OD) was irradiated at 365 nm wavelength with varying doses (250, 500, 750, and 1,000 J/cm$^2$), which delivers peak UVA-induced photon radiation absorbed by the cornea (5). Postirradiation, mouse corneal endothelial cell (MCEnC) morphology and density were assessed by in vivo confocal microscopy (Heidelberg retina tomograph [HRT]) at various time points after irradiation (Fig. 1*B* and *SI Appendix*, Fig. S1 *A–D*). The mouse CE showed a characteristic hexagonal monolayer with regular size and shape, consistent with the human endothelium (*SI Appendix*, Fig. S1 *B* and *C*) (21, 22). UVA induced fluence-dependent disruption of the monolayer, with reduction in cell density from ∼2,200 to ∼900 cells per square millimeter in a dose- and time-dependent manner within 2 mo postirradiation (Fig. 1 *C*, *Right* and *SI Appendix*, Fig. S1 *A–D*). Moreover, UVA caused formation of guttae-like lesions where drop-like bright "deposits" were surrounded by dark areas of lost cells (red arrowheads, Fig. 1*B*), comparable with the morphological changes seen in the human FECD cornea (red arrowheads, Fig. 1 *A*, *Right*).

Interestingly, we detected sex-dependent differences in MCEnC morphology and cell loss. While females had a sharp decline in the cell density with 500 J/cm$^2$, male mice did not show a significant decrease until 750 J/cm$^2$ at 2 mo compared to pre-UVA (Fig. 1*C*). Specifically, female mice showed exacerbated morphological changes, such as increased cell size and loss of discernible cell borders, as compared to males at the same recovery time points (Fig. 1*B*). After 500 J/cm$^2$, males retained the hexagonal monolayer configuration for up to 2 mo while females showed progressive disruption of the monolayer, with enlarged and irregular cells starting at 2 wk, and continued to display a more severe phenotype than males till a 3-mo time point. Similarly, after 1,000 J/cm$^2$, males showed discernible, although sicker, cells up to a 2-mo time point while females exhibited disorganized mosaic and loss of discernible cell junctions starting at 2 wk. Accordingly, females had 41% and 42% (500 J/cm$^2$) and 33% and 40% (750 J/cm$^2$) lower cell densities than males 1 and 2 mo after UVA, respectively (*SI Appendix*, Fig. S1*E* and Fig. 1*C*). At the 3-mo time point, progressive damage to the CE prevented reliable cell counts in vivo; thus, confocal images of tight junctions, immunostained ex vivo, were used for the morphometric analysis (Fig. 2*A*). After 3 mo, sex-dependent differences were present across all UVA doses, showing a decline in females by 24.5% (250 J/cm$^2$), 75.7% (500 J/cm$^2$), 60% (750 J/cm$^2$), and 57% (1,000 J/cm$^2$) compared to male mice (Fig. 2 *A*, *Right Graph*). Moreover, the hexagonality was 17% lower in females after 500 J/cm$^2$ (Fig. 2 *A*, *Left Graph*), and the coefficient of variation was greater by 56.5% (500 J/cm$^2$) and 47.0% (750 J/cm$^2$) in females as compared to males (Fig. 2 *A*, *Middle Graph*), indicating that females were more susceptible to UVA than male counterparts.

*N*-acetylcysteine (NAC) is an L-cysteine amino acid and a precursor to glutathione (GSH), known for its antioxidant and ROS scavenging properties (23). Since NAC has been shown to be cytoprotective in the COL8A2 mouse model of early-onset FECD (21), we tested the effect of NAC on UVA-induced MCEnC changes mimicking age-related FECD. The mice were fed with NAC 1 d prior to 1,000 J/cm$^2$ UVA irradiation and for 3 mo thereafter. Interestingly, we detected a 1.7-fold increase in MCEnC density in females (1,521 ± 313 for NAC vs. 855 ± 115 for no-NAC) and a 1.6-fold increase in males (1,560 ± 136 for NAC vs. 944 ± 136 for no-NAC) as compared with 1,000 J/cm$^2$ UVA irradiation only at 2 mo (Fig. 1*C*). Similarly, NAC supplementation significantly rescued both male and female endothelial cell density even at 3 mo after UVA, suggesting that ROS quenching restored UVA-induced cell loss (Fig. 2*A*).

**UVA Irradiation Increases Central Corneal Thickness to a Greater Extent in Females.** Corneal edema leads to an increase in central corneal thickness (CCT), which is a hallmark of endothelial cell functional impairment. The effect of UVA on MCEnC function was monitored by serial CCT measurements with in vivo OCT. Acutely, UVA irradiation led to the damage of the superficial corneal epithelium, (*SI Appendix*, Fig. S2*A*), leading to loss of epithelial barrier function and transient increase in CCT, not indicative of endothelial dysfunction. By 1 wk postirradiation, the epithelial defects healed (*SI Appendix*, Fig. S2*A*), and the CCT normalized to baseline for 500 and 750 J/cm$^2$ doses (Fig. 2 *B* and *C*); however, the second peak of CCT increase started at 1 mo after UVA for female mice (Fig. 2*B*) and at 2 to 3 mo for male

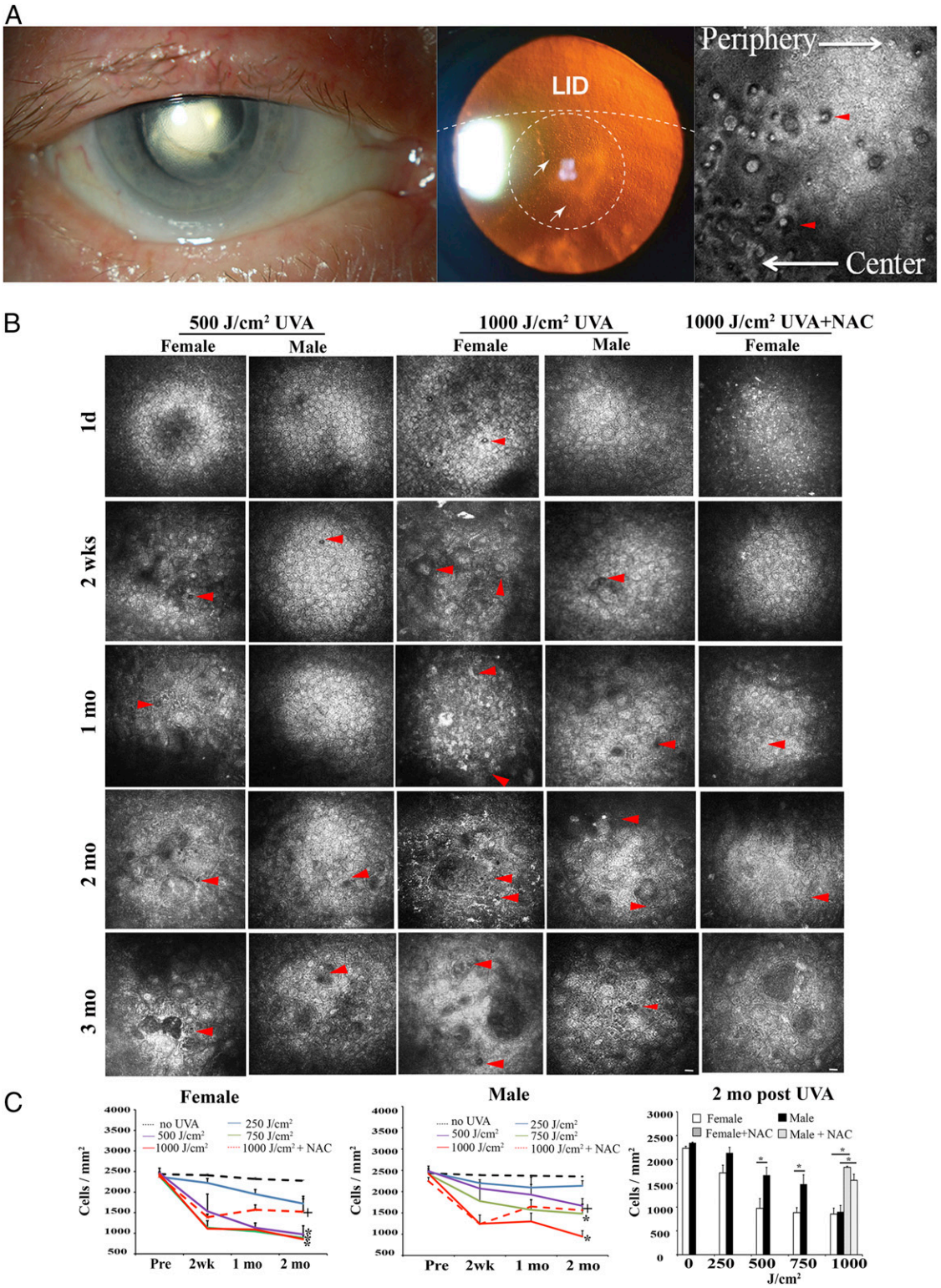


**Fig. 1.** UVA exposure causes progressive MCEnC morphological changes and decreases cell density. (*A*) Slit lamp images of FECD patient corneas are shown in the *Left* (broadbeam) and *Middle* (retroillumination) panels. White arrows indicate guttae, the dashed circle indicates the central cornea, and the white dashed line denotes the eyelid boundary. (*Right*) A corresponding HRT image of the patient cornea. Red arrowheads indicate guttae. (*B*) In vivo confocal HRT photographs of female and male MCEnCs with 500, 1,000 J/cm$^2$ UVA or 1,000 J/cm$^2$ UVA with NAC treatment at time points corresponding to 1 d, 2 wk, and 1, 2, and 3 mo post-UVA. (Scale bar, 100 μm.) (*C*) Cell density analysis of female (*Left*), male (*Middle*), and NAC-treated mice (*Right*) up to 2 mo post-UVA. $n = 4$ for 250, 500, or 750 J/cm$^2$ male or female treatments; $n = 13$ for male-1,000 J/cm$^2$ treatments; $n = 12$ for 1,000 J/cm$^2$ treatments in female mouse corneas; $n = 8$ for male-1,000 J/cm$^2$ with NAC treatment; $n = 7$ for female-1,000 J/cm$^2$ with NAC treatment. (*Left* and *Middle*) The * indicates the significant difference between UVA doses; the + denotes the significant difference between NAC- and non-NAC treatment ($P < 0.05$). (*Right*) The * indicates significant difference between the males and females or NAC and non-NAC treatment ($P < 0.05$).

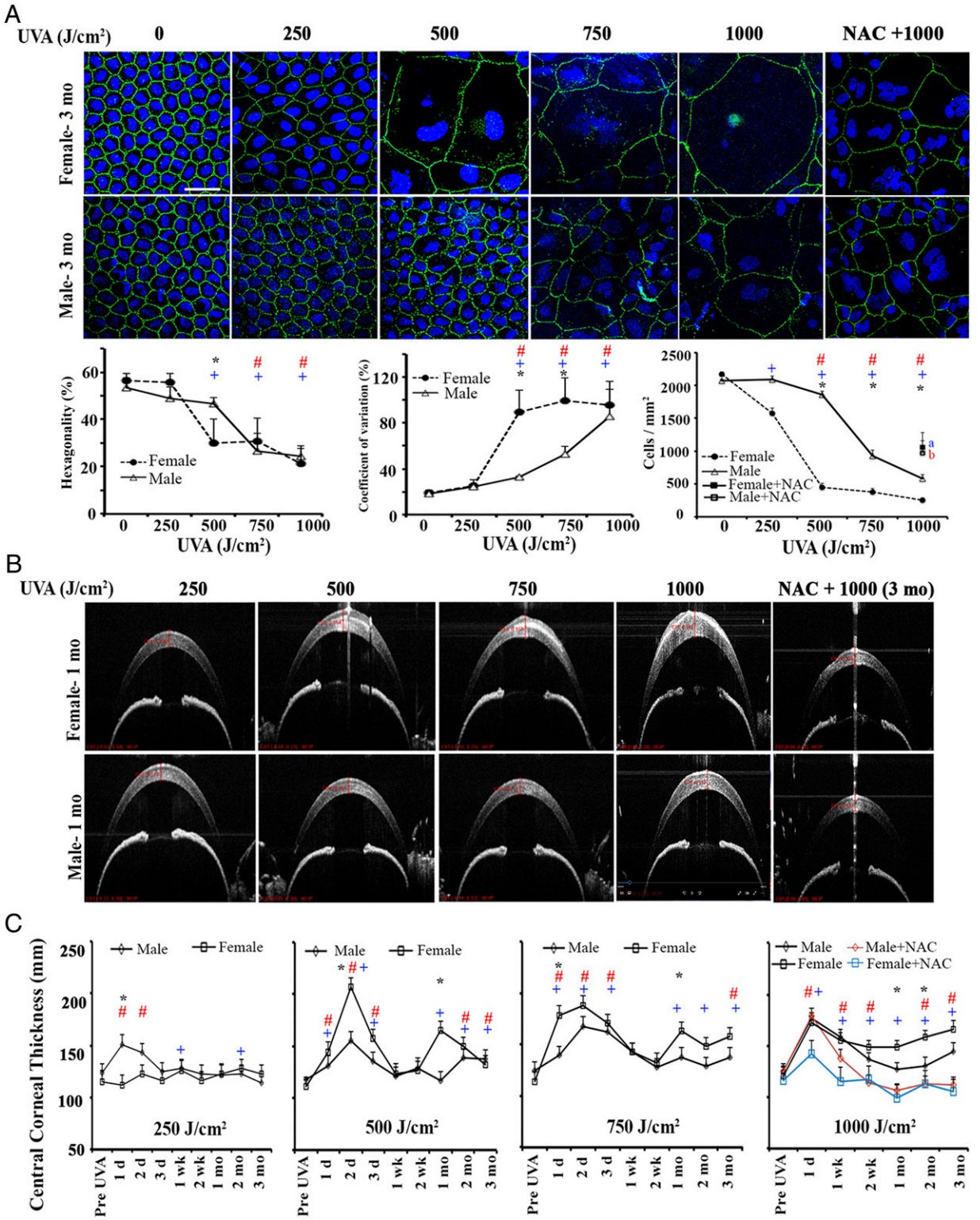


**Fig. 2.** UVA irradiation alters cell size and shape and modulates CCT. (*A, Upper*) Representative confocal images of whole mount of mouse MCEnCs detecting ZO-1 localization at 3 mo post-UVA. Shown are ZO-1 immunostaining-based analysis for hexagonality (*Lower Left*), coefficient of variation (*Lower Middle*), and cell density (*Lower Right*) for MCEnCs from females and males at 3 mo post-UVA ($n = 3$). Data are mean ± SEM. (Scale bar, 50 μm.) (*B*) Representative OCT images of mouse corneas at 1 mo post-UVA (female, *Upper*; male, *Lower*). (*C*) OCT image-based CCT analysis. Mixed-effect regression analysis was employed to analyze the effect of 250, 500, 750, and 1,000 J/cm$^2$ UVA, and 1,000 J/cm$^2$ UVA with NAC treatment on CCT changes. $n = 4$ for 250, 500, and 750 J/cm$^2$ UVA treatments; $n = 21$ and $n = 18$ for male and female 1,000 J/cm$^2$ treatment; $n = 8$ and $n = 6$ for NAC-treatment of male and females irradiated with 1,000 J/cm$^2$ UVA. Data are mean ± SEM; $P < 0.05$. The * represents the difference between non-NAC males and non-NAC females; the + represents the difference between post-UVA and pre-UVA for non-NAC females; the # represents the difference between post-UVA and pre-UVA for non-NAC males. The a and b indicate the difference in HRT between non-NAC and NAC-treated females and males 3 mo after 1,000 J/cm$^2$ UVA, respectively.

mice, indicating the induction of corneal edema (Fig. 2*C*) as a function of MCEnC loss (Fig. 2*A*). For the 1,000 J/cm$^2$ dose, even when epithelium healed (*SI Appendix*, Fig. S2*A*), corneal edema persisted (albeit improved from 1 d) and progressed for up to 3 mo, demonstrating a greater damage to the MCEnC function with a higher dose (Fig. 2*C*). Similar to the cell density findings (Fig. 2*A*), we detected a sex-dependent difference in CCT values. Females showed an earlier onset of endothelial function-related edema at 1 mo, with a 1.4-, 1.2-, or 1.2-fold increase in CCT for 500, 750, and 1,000 J/cm$^2$, respectively, compared to males (Fig. 2 *B* and *C*). The difference persisted up to a 2-mo time point after 1,000 J/cm$^2$ UVA, until both male and female corneas swelled to the same "maximal" point at 3 mo. Interestingly, the CCT of NAC-treated mice remained close to the untreated baseline at 1 to 3 mo after 1,000 J/cm$^2$ UVA without an induction of the second peak of edema, indicating the protective role of NAC on endothelial function (Fig. 2 *B* and *C*). NAC-treated males showed a significant decrease in CCT at 2 wk and 1 and 3 mo, and NAC-treated females showed a significant decrease in CCT at 1, 2, and 3 mo after 1,000 J/cm$^2$ UVA, as compared to 1,000 J/cm$^2$ treated males and females, respectively (Fig. 2 *C*, *Right Graph*). The histological feature of FECD is the thickening of Descemet's membrane (DM). Periodic acid–Schiff (PAS) staining revealed increased DM thickness from 2.1 ± 0.10 μm to 2.8 ± 0.28 μm and corneal edema at 3 mo after 1,000 J/cm$^2$ UVA (*SI Appendix*, Fig. S2 *B–F*). Similarly, transmission electron microscopy (TEM) images (*SI Appendix*, Fig. S2 *G–I*) showed thicker DM in UVA-treated eye as compared to controls.

**UVA Irradiation Induces Oxidative nDNA and mtDNA Damage Augmented in Female Mice.** To determine whether UVA affects the intraocular milieu abutting the CE (effects are ROS-dependent in vivo), we analyzed and compared the ROS production in the mouse and human aqueous humor (Fig. 3 *A–C*). Extracellular $H_2O_2$ levels in the aqueous humor showed a 4- and 11.6-fold increase in females and males, respectively, compared to those in control eyes (Fig. 3*A*). Furthermore, NAC supplementation significantly reduced ROS formed due to UVA (Fig. 3*B*). Similarly, aqueous fluid taken from FECD patients exhibited 2-fold heightened $H_2O_2$ levels, indicating a prooxidant milieu impacting FECD pathogenesis (Fig. 3*C*).

Furthermore, intense immunostaining with anti-8-OHdG (8-hydroxy-2′-deoxyguanosine), the marker of DNA oxidation, was detected in MCEnCs after UVA, recapitulating the findings of FECD ex vivo (22) (Fig. 3*D*). At 3 mo post-UVA, a terminal deoxynucleotidyltransferase-mediated dUTP nick end labeling (TUNEL) assay, which detects DNA fragmentation and apoptosis, showed 30% and 40% TUNEL-positive cells after 500 and 1,000 J/cm$^2$, respectively, in female mice while, in male mice, only 1,000 J/cm$^2$ induced TUNEL-positive apoptosis of 24% (Fig. 3 *E* and *F*). However, TUNEL-positive cells were not observed upon irradiation with 250 J/cm$^2$ UVA (*SI Appendix*, Fig. S3*A*). Specifically, UVA induced the formation of rosettes where apoptotic MCEnCs clustered around spaces of missing cells, similar to the pattern seen in FECD ex vivo. NAC-treated females and males showed significantly less TUNEL-positive cells as compared to non-NAC–treated UVA irradiated mice while NAC-treated males had fewer TUNEL-positive cells compared to NAC-treated females (Fig. 3*E*).

Next, we hypothesized that a differential response to the DNA damaging effects of UVA light might explain the sex-differences in the FECD phenotype. To test this, we performed long-amplicon PCR (LA-qPCR) analysis (24) (investigating the extent of nDNA and mtDNA damage) of MCEnCs during the FECD-phenotype development and compared the findings between female and male mice. The untreated contralateral eyes served as controls. The relative amplification of the small mtDNA fragment was employed as an estimate of mtDNA copy number (*SI Appendix*, Fig. S3*B*). UVA induced immediate mtDNA damage by decreasing amplification of mtDNA by 51% and 49% in female and male MCEnCs at 1 d, respectively (Fig. 3 *G* and *J*). The mtDNA damage recovered at a 2-wk time point for both sexes and then showed a second peak of damage, but only in females. Female mice exhibited a decrease in mtDNA amplification and an increase in lesion frequency at 1 mo (by 33%) and 3 mo (by 34%), demonstrating a 3.8- and 8.2-fold increase in mtDNA lesions per 10 kb compared to males at 1 and 3 mo, respectively. This suggested a secondary macromolecular damage occurring after the repair of the initial insult in females and not males.

The analysis of nDNA loci revealed that UVA induced a "delayed" damage starting only at the 1-mo time point where reduction in amplification of *Impdh* (by 49.7%, 0.78 lesions per 10 kb) and *Hprt* (by 70.5%, 1.37 lesions per 10 kb) occurred only in females (Fig. 3 *H–J*). At 3 mo post-UVA, amplification of *Impdh* reduced by 46.7% in females and by 27.5% in males. Similarly, amplification of *Hprt* declined by 44.3% in females and 40% for males. No nDNA sex differences were observed at 3 mo. However, with 1,000 J/cm$^2$ UVA at 3 mo, NAC treatment significantly rescued the nDNA damage in both sexes while mtDNA damage in females persisted even after NAC treatment (Fig. 3 *G–I*). Further, we sought to recapitulate the mtDNA damage noted in female mice in the immortalized human normal CE cell line (HCEnC-21T). We treated HCEnC-21T cells with the catechol estrogen 4-hydroxyestradiol (4-OHE$_2$) to mimic the female milieu in cells. We noted increased mtDNA lesions (0.65 DNA lesions per 10 kb) in HCEnC-21T cells at 24 h in comparison with 0.46 DNA lesions per 10 kb in the nuclear encoded β-globin gene (Fig. 3*K* and *SI Appendix*, Fig. S3 *C–E*).

To rule out the possibility that mtDNA damage is due to impaired mitophagy where lack of clearance of dysfunctional mitochondria leads to persistent DNA damage, we performed ultrastructural analysis of MCEnCs (25). TEM showed an increase in the number and size of vacuoles containing mitochondria (arrows, Fig. 3 *L–N*), indicative of a heightened formation of autophagic structures in UVA-treated MCEnCs compared to controls. Moreover, levels of autophagy marker LC3-I to -II were increased after 1,000 J/cm$^2$ UVA (*SI Appendix*, Fig. S3*F*), more so in females than males, and the levels of small mtDNA copy number (measure of mitochondrial content) were mostly constant, except for a small decrease in females at 3 mo. Therefore, UVA did activate auto/mitophagy, as seen in FECD (26–28), demonstrating that lack of ability to remove damaged mitochondria was likely not the cause for the increased mtDNA damage after UVA-induced stress.

**UVA Irradiation Elevates CYP1B1 and Promotes Estrogen-DNA Adduct Formation in Female Mice.** Based on the findings of a more severe UVA-induced phenotype in female mice, we investigated whether estrogen metabolism is involved in FECD development (Fig. 4*A*). Specifically, we aimed to explore the role of CYP1B1 and CYP1A1 (Schematic, Fig. 4*A*), the major estrogen-metabolizing enzymes that trigger the estrogen genotoxic pathway, in accounting for the sex differences in FECD phenotype. Strikingly, we noted significant up-regulation of both CYP1B1 and CYP1A1 protein levels in FECD ex vivo patient specimens compared to donor corneal tissues (Fig. 4*B* and *SI Appendix*, Fig. S4*A*). Next, we investigated whether UVA induced CYP1B1 in vitro in CE cells. We treated normal CE cells with 5 J/cm$^2$ UVA and assessed CYP1B1 protein levels at 7 and 24 h postirradiation. CYP1B1 was significantly up-regulated (3-fold) in vitro 24 h after UVA (Fig. 4*C*). TCDD (2,3,7,8-tetrachlorodibenzo-p-dioxin), an aryl hydrocarbon receptor agonist, served as positive control for CYP1B1 induction (Fig. 4*C*). In addition to its localization in the endoplasmic reticulum, CYP1B1 is also bimodally targeted to mitochondria via its N-terminal mitochondria localization signal sequences (29). We investigated the subcellular localization of CYP1B1 in normal

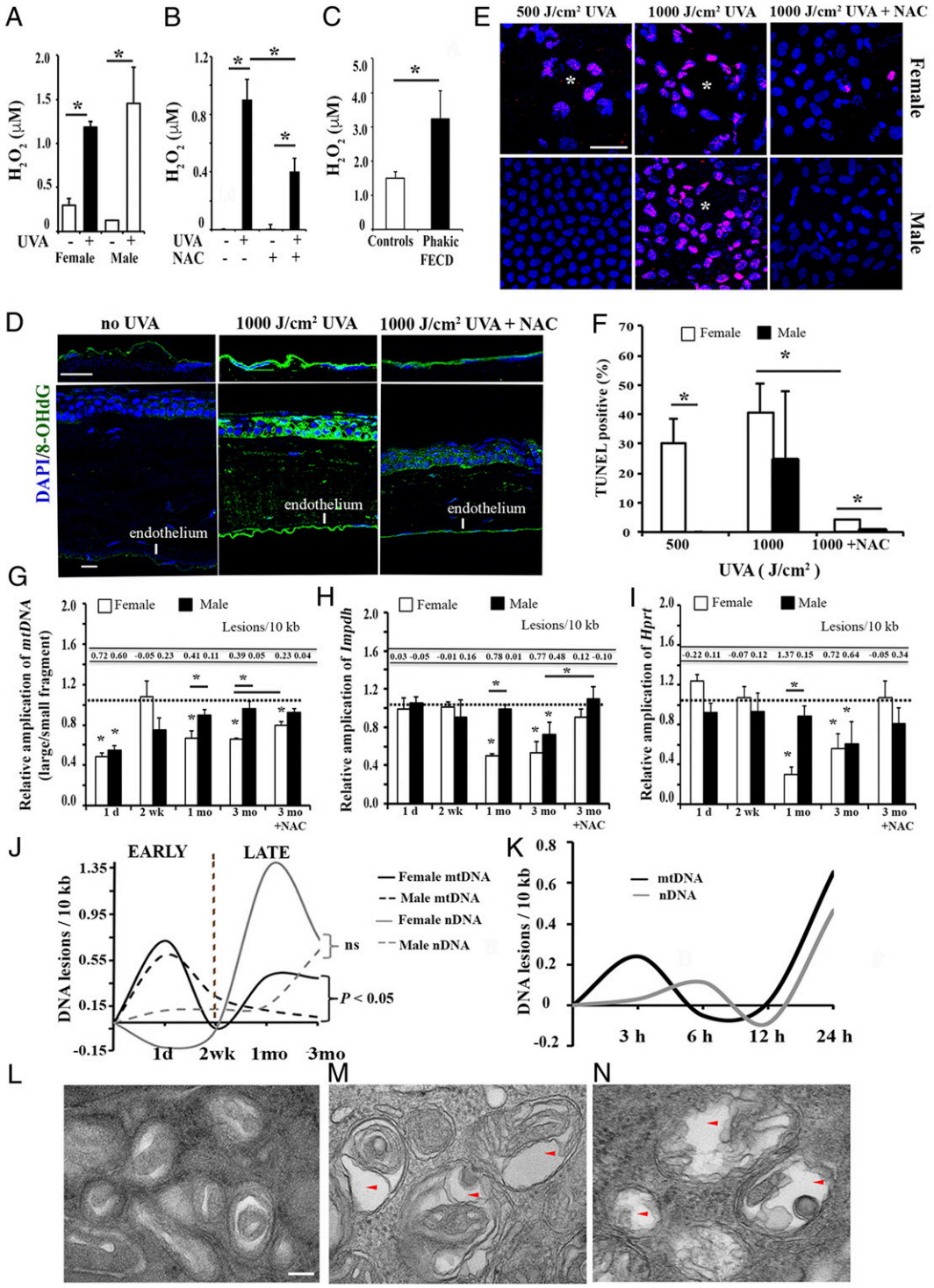


**Fig. 3.** UVA irradiation induces ROS, DNA damage, mitochondria swelling, and cell apoptosis in MCEnCs. (*A*) $H_2O_2$-based ROS production in the aqueous humor from 1,000 J/cm$^2$ UVA-treated eyes immediately post-UVA ($n = 3$) and control eyes. (*B*) ROS production in the aqueous humor from mice with or without NAC treatment 1 d post-UVA ($n = 4$). (*C*) $H_2O_2$-based ROS production in the aqueous humor from phakic FECD (with native lens) patients ($n = 7$) and controls (cataract patients, $n = 16$). *$P < 0.05$, Student's *t* test. (*D*) Representative confocal images of whole mount of the mouse CE with 8-OHdG (green) labeling 3 mo after 1,000 J/cm$^2$ UVA. DAPI was used for nuclei staining (blue). (Scale bars, 50 μM.) (*E* and *F*) Representative confocal images of whole mount of the female (*Upper*) and male (*Lower*) mouse CE with TUNEL labeling (pink) 3 mo after 500 J/cm$^2$ or 1,000 J/cm$^2$ UVA and the corresponding quantification of percent TUNEL-positive cells. DAPI was used for nuclei staining (blue). White asterisks indicate rosette formation. (Scale bar, 50 μm.) *$P < 0.05$, Student's *t* test. Detection of MCEnC mtDNA (*G*), nDNA (*H* and *I*) damage, and DNA lesions using LA-qPCR analysis. The horizontal dotted lines in *G*–*I* indicate the normalization of the corresponding untreated OS eye for each time point to 1. Data are mean ± SEM, *$P < 0.05$ by 2-way ANOVA. (*J*) Graphical representation of the mtDNA (black) and nDNA lesions (gray) in female (solid line) and male (dashed line) MCEnCs from 1 d to 3 mo after 1,000 J/cm$^2$ UVA. "ns" indicates nonsignificant. (*K*) Graphical illustration of the mtDNA (black) and nDNA lesions (gray) in normal HCEnC-21T cells upon 15 μM 4-$OHE_2$ treatment for varying time points. (*L*–*N*) Representative TEM images of mitochondrial changes in MCEnCs of mouse corneas without UVA (*L*, female; magnification: 98,000×) or with 1,000 J/cm$^2$ UVA at 3 mo (*M*, female, *N*, male; magnification: 98,000×). The red arrowheads indicate the autophagic vacuolar structures in MCEnCs. (Scale bar, 100 nm.)

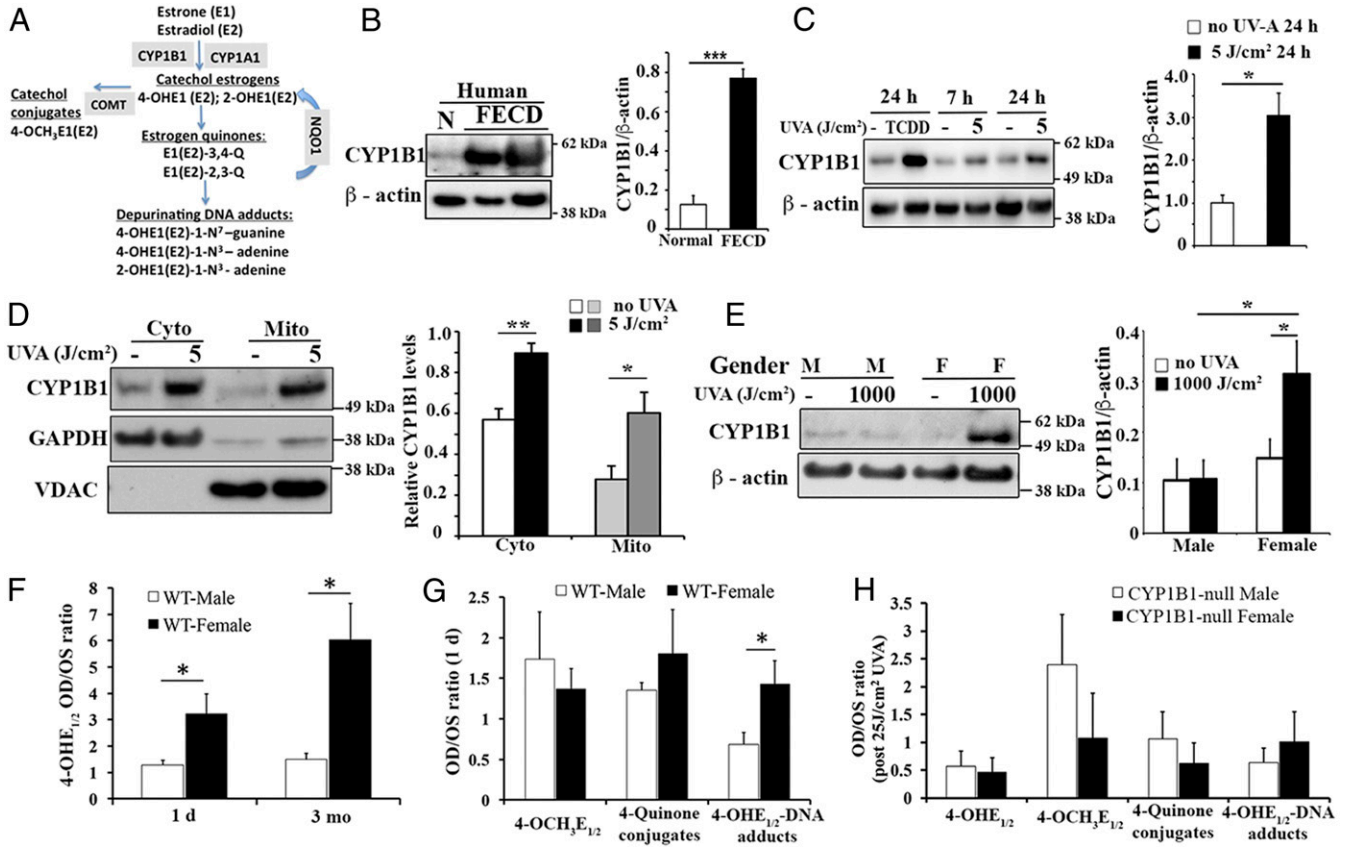


**Fig. 4.** UVA irradiation induces estrogen metabolites in females via enhanced expression levels of CYP1B1. (*A*) Schematic illustration of the catechol estrogen metabolic pathway and generation of estrogen-DNA adducts. (*B*) Representative Western blot of CYP1B1 in normal ($n = 5$) and FECD ($n = 9$) specimens. β-actin serves as normalizing control. Densitometry analysis of the enzyme levels is indicated in the *Right* as bar graphs. ***$P < 0.001$, 2-tailed Student's *t* test. (*C*) In vitro Western blotting analysis of CYP1B1 levels in UVA-irradiated immortalized normal CE cells after 7 and 24 h after 5 J/cm$^2$ irradiation ($n = 3$). Treatment with 30 nM TCDD was used as positive control for CYP1B1 induction. Densitometric analysis of CYP1B1 is indicated as bar graph. *$P < 0.05$, 2-tailed Student's *t* test. (*D*) Western blotting of CYP1B1 levels in the cytoplasmic and mitochondrial fractions extracted from normal CE cells 24 h after 5 J/cm$^2$ irradiation ($n = 4$). Voltage-dependent anion-selective channel (VDAC) and glyceraldehyde 3-phosphate dehydrogenase (GAPDH) served as mitochondrial and cytoplasmic fraction controls, respectively. Densitometric analysis of CYP1B1 normalized to GAPDH (cyto) and VDAC (mito) are indicated as bar graph to the *Right*. *$P < 0.05$, **$P < 0.01$, 2-tailed Student's *t* test. (*E*) CYP1B1 Western blot in MCEnCs at 1 d after 1,000 J/cm$^2$ UVA. Densitometric analysis of CYP1B1 ($n = 3$ for males, $n = 4$ for females) levels is indicated as bar graphs. *$P < 0.05$, 2-tailed Student's *t* test. (*F*) Quantitative analysis of 4-OHE$_{1/2}$ levels in the mouse CE 1 d and 3 mo after 1,000 J/cm$^2$ UVA. The accumulation of 4-OHE$_{1/2}$ is represented as the ratio of OD (treated eye) by OS (untreated eye). White and black bars represent WT male ($n = 6$ for 1 d, $n = 4$ for 3 mo) and female ($n = 7$ for 1 d, $n = 4$ for 3 mo) mice, respectively. *$P < 0.05$, 2-tailed Student's *t* test. (*G*) Ratio of levels of 4-OCH3E$_{1/2}$, 4-quinone conjugates, and 4-OHE$_{1/2}$-DNA adducts 1 d after 1,000 J/cm$^2$ UVA. White and black bars represent WT male ($n = 7$) and female ($n = 9$) mice, respectively. *$P < 0.05$, 2-tailed Student's *t* test. (*H*) OD/OS ratio of 4-OHE$_{1/2}$, 4-OCH3E$_{1/2}$, 4-quinone conjugates, and 4-OHE$_{1/2}$-DNA adducts in CYP1B1-null mice after ex vivo treatment of corneal cups with 25 J/cm$^2$ UVA. White and black bars represent CYP1B1-null mice male ($n = 5$) and female ($n = 5$), respectively.

CE cells upon UVA. CYP1B1 expression increased in the mitochondrial fraction (2.1-fold) along with the cytoplasmic fraction (1.5-fold) 24 h after 5 J/cm$^2$ UVA (Fig. 4*D*), suggesting possible UVA-mediated mitochondrial translocation of CYP1B1. Furthermore, we assessed CYP1B1 levels in our in vivo UVA model. Interestingly, 1,000 J/cm$^2$ UVA irradiation led to 3-fold up-regulation of CYP1B1 in female but not in male mice 1 d post-UVA (Fig. 4*E*). Similarly, CYP1B1 was up-regulated in female mice with all UVA doses at 3 mo post-UVA, compared to males (*SI Appendix*, Fig. S4*B*).

Since CYP1B1 drives the conversion of $E_{1/2}$ into 4-OHE$_{1/2}$ followed by the generation of catechol estrogen quinones and depurinating DNA adducts (Fig. 4*A*), we analyzed these estrogen metabolites in the mouse cornea by ultra performance liquid chromatography followed by tandem mass spectrometry (UPLC/MS-MS). To evaluate the changes in levels of estrogen metabolites induced by UVA, we used the ratio of each metabolite from UVA-treated (OD eye) to the nontreated (OS eye) samples. Supporting the increased CYP1B1 expression upon UVA, a significant increase in the ratio of 4-OHE$_{1/2}$ was noted in females at both 1 d and 3 mo post-UVA (Fig. 4*F*). This accumulated 4-OHE$_{1/2}$ can either be neutralized by the COMT enzyme to methoxy catechol estrogens or be driven toward forming estrogen quinones that later form depurinating DNA adducts (Fig. 4*A*). COMT levels remained unchanged in both males and females 1 d post-UVA (*SI Appendix*, Fig. S5*A*). Consistently, 4-methoxy estrogen (4-OCH$_3$E$_{1/2}$) levels also remained unchanged between males and females 1 d postirradiation (Fig. 4*G*). Therefore, the increased levels of 4-OHE$_{1/2}$-DNA adducts observed in females 1 d postirradiation (Fig. 4*G*) indicate that the accumulated 4-OHE$_{1/2}$ is driven toward generation of depurinating DNA adducts over its neutralization. We did not detect significant levels of depurinating DNA adducts 3 mo postirradiation, owing to the instability of these adducts being released immediately to the aqueous humor surrounding the endothelial cells and further eliminated from the body. Overall, we speculate that the up-regulation of CYP1B1 in ex vivo human FECD specimens could

be potentially due to impaired sex hormone pathways in these patients, an underexplored avenue in FECD pathogenesis.

In contrast to CYP1B1, although CYP1A1 levels were up-regulated 1 d post-UV irradiation in vivo, the extent of increase was mostly similar between males and females (*SI Appendix*, Fig. S4*C*). The ratios of corresponding 2-hydroxyestradiol (2-$OHE_{1/2}$) and 2-$OHE_{1/2}$-DNA adducts were not significantly different between males and females (*SI Appendix*, Fig. S4*E*) after 1 d of irradiation. Therefore, the increase in 4-$OHE_{1/2}$-DNA adducts seen in females (Fig. 4*G*) indicates that the majority of estrogen in females is utilized by the increased CYP1B1 driving it to the 4-OHE pathway. Hence, less substrate is available for CYP1A1 to form metabolites in the 2-OHE pathway. This is consistent with the decrease in the 2-$OHE_{1/2}$ ratio (*SI Appendix*, Fig. S4*F*) with a concomitant increase in the 4-$OHE_{1/2}$ ratio (Fig. 4*F*) in females compared to males at 3 mo post-UVA. The significance of these observations is strengthened by a previous study which showed that more DNA adducts are formed from 4-$OHE_{1/2}$, thereby forming apurinic sites compared to those formed from 2-$OHE_{1/2}$ (30). Three months after irradiation, CYP1A1 expression did not show significant changes in male and female mice upon UVA (*SI Appendix*, Fig. S4*D*).

Furthermore, to investigate the importance of differential expression of CYP1B1 in female and male mice, we utilized CYP1B1-null mice for UVA-based studies (31). The cornea of CYP1B1-null mice was treated ex vivo with 25 J/$cm^2$ UVA and harvested for estrogen metabolite analysis as described above. UVA irradiation did not increase the ratio of 4-$OHE_{1/2}$ in either male or female CYP1B1-null mice (Fig. 4*H*). Similarly, we did not observe any changes in the levels of 4-$OHE_{1/2}$-DNA adducts upon UVA in CYP1B1-null mice (Fig. 4*H*). Collectively, these data strengthen our hypothesis that differential up-regulation of CYP1B1 in female mice in the UVA model leads to derailed endogenous estrogen metabolism. This causes accumulation of depurinating DNA adducts modeling the DNA damage noted in FECD and provides mechanistic insights on the increased prevalence of FECD in females.

## Discussion

FECD is a complex disorder, resulting from the multifactorial interplay of genes and environment. Although multiple genetic associations have been described (32–36), this study points to an important environmental factor involved in FECD development, adding to the body of evidence on the etiology and possible prevention of this common corneal condition. Lack of an in vivo model has impeded the studies on FECD pathophysiology and interventions to inhibit its progression. FECD is a genetically heterogeneous disease associated with mutations of multiple genes and manifests in 2 forms: early-onset and late-onset, the latter being more prevalent (37). Unlike late-onset FECD, which is predominant in females, early-onset FECD occurs equally in both sexes in a 1:1 ratio (38). Missense mutations in the gene encoding the α2 chain of Collagen VIII (*COL8A2*) have been shown to be associated with the early-onset form of FECD (36, 38), as corroborated by the knock-in mouse model (21, 28). Intronic CTG repeat expansion in the *TCF4* gene is the most common genetic marker associated with late-onset FECD that is inherited in an autosomal dominant fashion (39). Apart from *TCF4*, mutations in *KANK4*, *LAMC1*, *ATP1B1*, *SLC4A11*, *LOXHD1*, *ZEB1*, and *AGBL1* have been shown to be associated with FECD (33–35, 40). A recent genome-wide association study identified sex-specific association for *LAMC1* and *TCF4* in FECD patients (33). Regardless of late-onset FECD genotype, the outcome is susceptibility to oxidative stress (4, 10, 22, 41). The CE is exposed to UV light throughout life and is susceptible to acquired oxidative damage. We based the development of the late-onset and age-related form of the FECD model on the physiological outcome of this susceptibility. This study shows that UV light causes FECD, providing evidence of the environmental influences involved in FECD development. Further studies are needed to investigate the interplay between genetic and environmental factors involved in female susceptibility in developing FECD.

We previously showed that UVA activates the Nrf-2–mediated antioxidant pathway and induces apoptosis in corneal endothelial cells in vitro (42). A recent study demonstrated that UVA irradiation (600 J/$cm^2$) of rabbit corneas ex vivo increased redox imbalance in the endothelium compared to the outermost epithelial layer, rendering endothelial cells more susceptible to UVA-induced oxidative damage (6). Safety studies for corneal cross-linking studies done in rabbits have determined that high doses of UVA are cytotoxic to corneal endothelial cells (43, 44). In this study, we simulated the life-long exposure of endothelium to UV light by using high-dose UVA irradiation (1,000 J/$cm^2$) and detected progressive degenerative effects of UVA-mediated damage, modeling FECD in vivo. While exposure to UV is a known factor in other ocular pathologies, including photokeratitis (45, 46), which leads to corneal epithelial damage, in our study, the immediate epithelial defects after irradiation healed within 1 wk. Even though photokeratitis is known to result in endothelial dysfunction (47), these patients do not necessarily develop FECD. The genetic component likely renders the FECD endothelium more susceptible to UVA, and the susceptibility is amplified herein with exposure of mouse corneas to high doses of UVA.

We have detected greater susceptibility of female mice to UVA by showing greater CE cell loss and more prominent morphological changes, as compared to male mice. Moreover, corneal edema was more prominent in female mice, consistent with the epidemiologic studies that have shown other prooxidant factors, such as diabetes and smoking, having a more pronounced effect on the development of corneal edema and FECD progression in female cohorts (15). At the molecular level, female mice showed greater nDNA damage as compared to male mice at a 1-mo time point after UVA, correlating with a lower CE cell number and higher CCT in females. At 3 mo, both female and male mice exhibited nDNA damage, indicating development of a fairly similar "end-stage" phenotype in both males and females. However, mtDNA damage, which was induced immediately after UVA irradiation, was repaired at 2 wk and then showed a "secondary" increase only in females at 1 and 3 mo. This reappearance of mtDNA damage only in females likely explains the differential response to UVA between the sexes. Similarly, FECD human specimens exhibited marked reduction in mtDNA amplification, indicating accumulation of basal DNA damage and subsequent mitochondrial dysfunction (10). However, temporal investigation of the animal model provides insight into the possible mechanism at the earlier stages of the disease formation (21) and sheds light on the mechanism of sex differences in FECD that were not explored in previous studies.

Differential susceptibility to UVA between females and males was accompanied by up-regulation of CYP1B1 in female but not male mice at early and late time points after UVA. Previous studies showed up-regulation of CYP1B1 and CYP1A1 in zebrafish (48) and in rats (49) with combined UVA and UVB exposure; however, this study shows that targeted induction of CYP1B1 preferentially in female mice was achieved by in vivo irradiation of the postmitotic ocular tissue with UVA alone, causing CYP1B1-mediated estrogen genotoxicity. Oxidation of tryptophan by UVA irradiation results in the formation of photoproducts that are aryl hydrocarbon receptor (AHR) agonists, thereby inducing CYP1B1 in a human keratinocyte cell line (50). Mutations in CYP1B1 have been reported as the major genetic determinant of primary congenital glaucoma (51). Of interest is the heightened mtDNA damage seen in female mice that is consistent with mitochondrial targeting of CYP1B1 causing oxidative damage to mitochondria (52). The mtDNA is specifically prone to oxidative damage due to lack of protective histones

and propagation of ROS-induced lipid peroxidation in the inner mitochondrial membrane (53). Moreover, mtDNA has been shown to be more susceptible to covalent modification by estrogens and formation of estrogen-DNA adducts than nDNA (54, 55), leading to obstruction of mitochondrial gene replication as previously detected in FECD (10, 56). Furthermore, our data showed greater accumulation of depurinating DNA adducts stemming from 4-$OHE_1(E_2)$ catechol estrogens as compared to 2-$OHE_1(E_2)$, consistent with greater activation of CYP1B1. The redox cycling of estrogen quinone derivatives from 4-$OHE_1(E_2)$ catechol estrogens has been shown to produce higher levels of depurinating (as opposed to stable) adducts (57), correlating with greater formation of estrogen-driven tumors (17, 18). Higher levels of estrogen DNA adducts are associated with Parkinson's disease and breast cancer, and genetic polymorphisms in CYP1B1 leading to higher adducts are associated with ovarian cancer (58–60). This study provides insights into estrogen metabolism having a physiological relevance in the degenerative loss of postmitotic cells in vivo.

## Materials and Methods

**Experimental Animals.** C57BL/6 wild-type mice (male and female, 7 to 15 wk old; The Jackson Laboratory or Charles River) were used for this study. Mice were housed in a climate-controlled animal facility at the Schepens Eye Research Institute (Boston) and kept under cyclic light conditions with 12 h ON or OFF. Mice were anesthetized with a combined dose of ketamine (100 mg/kg) and xylazine (20 mg/kg) administered intraperitoneally. Female mice were irradiated at proestrus stage (61). For the NAC-treated group, mice were fed daily with drinking water containing 1 g of NAC/kg body weight from 1 d prior up to 3 mo post-UVA. All animal experiments were approved by the Institutional Animal Care and Use Committee and adhered to the ARVO Statement for the Use of Animals in Ophthalmic and Vision Research.

**Human Corneal Endothelial Cell Culture.** Telomerase and SV40 T antigen immortalized normal human CE cell lines HCEnC-21T and HCEnC-SV-67F-16, respectively, were previously generated in our laboratory (26, 62). HCEnC-21T cells were seeded in estrogen-free medium (phenol red-free OptiMEM-I; Thermo Fisher Scientific) with charcoal stripped FBS (HyClone), 200 mg/L calcium chloride (Sigma-Aldrich), 0.08% chondroitin sulfate (Sigma-Aldrich) and treated with 15 μM 4-$OHE_2$ (Steraloids) in phenol red-free OptiMEM-I.

**UVA Irradiation of Mouse Cornea.** A UVA LED light source (M365LP1; Thorlabs) with an emission peak of 365 nm light, 9 nm bandwidth (FWHM) and irradiance of 398 mW/$cm^2$ was focused to illuminate a 4-mm-diameter spot onto the mouse cornea. The energy was measured using a laser sensor (model L49 [150A]; Ophir) ,and the time of UVA exposure was adjusted to deliver the appropriate fluence (10 min 29 s for 250 J/$cm^2$, 20 min 57 s for 500 J/$cm^2$, 31 min 26 s for 750 J/$cm^2$, and 41 min 54 s for 1,000 J/$cm^2$). The right eye (OD) was irradiated while the contralateral eye (OS) was covered with heat retention drapes (SpaceDrapes, Inc.) to serve as untreated control.

Mouse eyeballs from CYP1B1-null mice (age 8 to 12 wk, 10 females and 10 males) (31) were enucleated, rinsed with phosphate-buffered saline (PBS), and transported on ice, and cornea excision was performed within 24 h of the animal's death. Four 12-inch RPR-3500A UVA tubes (The Southern New England UV Co.) emitting 350 nm light (irradiance: 7.13 mW/$cm^2$) were used to irradiate the corneoscleral buttons placed in sterile PBS, with the endothelial side facing the source. The fluence delivered was 25 J/$cm^2$ (58 min 24 s at a distance of 10 cm). Irradiated corneas were snap-frozen, homogenized using a tissue grinder ,and dissolved in methanol:water (2:1) for estrogen metabolite analysis.

**UVA Irradiation of CE Cell Lines In Vitro.** Two 19.5-inch UVA tubes (XX-15L; Analytik Jena US LLC) emitting 365 nm light (irradiance: 14.77 mW/$cm^2$) were used to irradiate normal CE cells in 12-well cell culture plates in estrogen-free Chens medium. The fluence delivered was 5 J/$cm^2$ (5 min 33 s at a distance of 10 cm from the light source). After irradiation, cells were allowed to recover in the same medium and harvested at 7 h and 24 h.

**In Vivo Imaging.** After anesthetizing, mouse corneal images were taken using a slit-lamp biomicroscope with a camera (Nikon D100, Tokyo). Fluorescein (1 μL in 2.5% in PBS; Sigma-Aldrich) was topically applied onto the mice lateral conjunctival sac to assess the epithelial cell integrity by observing punctate staining under cobalt blue light. Anterior segment images were taken using anterior segment–optical coherence tomography (OCT) (Bioptigen Spectral Domain Ophthalmic Imaging System Envisu R2200 with 12 mm telecentric lens to scan the cornea; Bioptigen). CCT was measured using inbuilt software.

The mouse was wrapped with heat retention drapes on the platform that holds the mouse body securely for imaging CE cells by laser scanning IVCM using the Heidelberg Retina Tomograph III (HRT III) with Rostock Corneal Module (RCM) (Heidelberg Engineering). The laser confocal microscope acquires 2D images that represent a coronal section of the cornea of 400 × 400 μm (160,000 $μm^2$) at a selectable corneal depth. Acquired images comprise 384 × 384 pixels and with a lateral resolution of 1 μm per pixel. Digital images were stored on a computer workstation at 3 frames per second.

**Analysis of CE Cell Density.** The CE density of HRT images acquired before UVA and post-UVA at 2 wk and 1 and 2 mo was analyzed by a semiautomated cell counter in the software Heidelberg Eye Explorer, version 1.3.0 (Heidelberg Engineering GmbH) inbuilt in HRT3. The mean cell density was calculated from 3 mice whose HRT images were counted by at least 2 observers. For each image, an area with at least 50 cells was selected. For CE density calculated from the images of 3 mice with ZO-1 immunostaining, cell count was performed manually by 2 blinded observers using a plug-in for ImageJ 1.46r (https://imagescience.org/meijering/software/imagescience; provided in the public domain by Wayne Rasband, NIH). Cell density was normalized to the area of each image in square millimeters.

**Analysis of CE Morphology.** CE images captured from whole mount ZO-1 immunostaining and uploaded into Confoscan 4 software (NIDEK Technologies, Padua, Italy). The magnification of confocal ZO-1 images used for Confoscan is 40× with zoom 2. Automatic cell analysis was performed after boundaries of the cells were decided. CE polymegethism (variation in cell size) and pleomorphism (variation in cell shape) were calculated. Mean polymegethism and pleomorphism were calculated from 3 images.

**Immunocytochemistry and Histology.** A dissected mouse cornea cup was fixed with 70% ethanol (ZO-1) or 4% PFA (TUNEL) for 30 min at room temperature. For ZO-1 staining, the cornea cup was permeabilized with 0.2% Triton X-100 in PBS for 10 min and blocked in 2% bovine serum albumin (BSA)-PBS for 15 to 30 min. The cornea cup was incubated with anti-ZO-1 antibody (339100; Thermo Fisher Scientific) in 4% BSA-PBS at 4 °C overnight and with secondary anti-rabbit fluorescein isothiocyanate (FITC) or anti-goat FITC (AB_2315776 or AB_2340401; Jackson Immunoresearch Labs) for 1 h. For the TUNEL assay, an In Situ Cell Death Detection Kit (Roche Diagnostics GmbH) was used according to the manufacturer's instructions. A corneal cup was incubated with TUNEL for 1 h at 37 °C followed by 4 washes with PBS, 10 min each. The corneal cup was flattened by 3 to 4 radial cuts and mounted using DAPI mounting medium (H-1200; Vector Labs). For 8-OHdG-immunostaining, the eyeballs were enucleated and fixed in 10% formalin, embedded in paraffin, sectioned, and stained with anti–8-OHdG (AB5830; Millipore Sigma) overnight at 4 °C and with secondary antibody anti-goat FITC for 1 h. Digital images were obtained using a spectral photometric confocal microscope (DM6000S with LCS 1.3.1 software; Leica). ZO-1–based cell count and TUNEL positive cells were counted by blinded observers using the plug-in for ImageJ 1.46r (https://imagescience.org/meijering/software/imagescience; provided in the public domain by Wayne Rasband, NIH, Bethesda, MD).

**ROS Production Assay.** Extracellular $H_2O_2$ levels in the mouse aqueous humor (3 μL), collected using a capillary needle from the dilated mouse anterior chamber, were detected using the Amplex Red Assay Kit (Molecular Probes, Life Technologies) according to manufacturer's instructions. Fluorescence was measured with excitation and emission at 550 and 590 nm, respectively, using a microplate reader (Bio-Tek) with Gen5 software at 37 °C.

**DNA Damage Analysis Using LA-qPCR.** Mouse CEs with DM were dissected from a corneal cup and followed by genomic DNA extraction using Qiagen DNeasy Blood and Tissue Kit (Qiagen). LA-qPCR analysis for mtDNA and nDNA was performed as previously described (24). Genomic DNA was isolated from HCEnC-21T cells treated with 4-$OHE_2$ using Genomic tip-20/G (Qiagen). DNA lesion frequencies were calculated as described (24). Two-way analysis of variance (ANOVA) was utilized for statistical analysis, with $P$ values corresponding to $<0.05$ (*) as significant.

**Estrogen Metabolite Analysis.** Immediately after euthanizing mice 1 d post-UVA treatment, the corneal cups were dissected, followed by storage at –80 °C. Two

corneal cups with the same sex and treatment were pooled into one. Frozen corneal cups (2 each) were ground using liquid nitrogen and extracted with methanol/water (1:1, 3×). Fractions were pooled and concentrated using Speed-Vac and lyophilized. The residue was resuspended in 70 μL of methanol/water 1:1 with 0.1% formic acid and filtered through a 5,000-molecular weight cutoff filter (Millipore) before analysis by ultraperformance liquid chromatography/tandem mass spectrometry (UPLC/MS/MS).

All of the samples were analyzed on a Waters Acquity UPLC equipped with a MicroMass QuattroMicro triple stage quadrupole mass spectrometer (UPLC/MS/MS; Waters). The 10-μL injections were carried out on a Waters Acquity UPLC $BEHC_{18}$ column (1.7 μm, 10 × 100 mm). The instrument was operated in positive electrospray ionization mode. All aspects of system operation, data acquisition, and processing were controlled using QuanLynx v4.2 software (Waters). The column was eluted starting with 20% acetonitrile in water (0.1% formic acid) for 4 min at a flow rate of 150 μL/min, then to 55% acetonitrile in 10 min. Ionization was achieved using the following settings: capillary voltage 3 kV; cone voltage 15 to 40 V; source block temperature 120 °C; desolvation temperature 200 °C, with a nitrogen flow of 700 L/h. Five-point calibration curves were run for each standard, and data were quantified by comparison with known amounts of standards as described previously (63). The results were compared between groups using Student's *t* test.

See *SI Appendix, Materials and Methods* for detailed experimental procedures for HRT and TEM imaging. Details of the mitochondrial fractionation and antibodies used for Western blotting are also provided in *SI Appendix*.

**Data Availability.** All data discussed in the paper are already available in the manuscript or *SI Appendix*.

**ACKNOWLEDGMENTS.** We deeply acknowledge Prof. Irene Kochevar and Bill A. Farinelli (Wellman Center for Photomedicine, Massachusetts General Hospital, Harvard Medical School, Boston) for their expertise and help in setting up the UVA lamp assembly for in vivo irradiation. CYP1B1-null mouse corneas were kindly gifted by Dr. Frank J. Gonzalez (NIH). This work was supported by NIH/National Eye Institute Grant R01EY020581 (to U.V.J.), an Alcon Young Investigator Grant (to U.V.J.), Core Grant P30EY003790, a Research to Prevent Blindness Award (to U.V.J.), an Alcon Research Institute Young Investigator Award (to U.V.J.), the New England Corneal Transplant Research Fund (U.V.J.), a Japan Eye Bank Association Overseas Grant (to T. Miyajima), a Bausch and Lomb Ocular Surface Research Fellowship (to T. Miyai), a Japan Eye Bank Association Overseas Grant (to T. Miyai), a Nakayama Foundation International Exchange Grant (to T. Miyai), American Heart Association Postdoctoral Fellowship 18POST34030385 (to V.K.), and a Shire Research Scholarship (to S.O.T.).

1. N. C. Joyce, Proliferative capacity of the corneal endothelium. *Prog. Retin. Eye Res.* **22**, 359–389 (2003).
2. N. C. Joyce, C. C. Zhu, D. L. Harris, Relationship among oxidative stress, DNA damage, and proliferative capacity in human corneal endothelium. *Invest. Ophthalmol. Vis. Sci.* **50**, 2116–2122 (2009).
3. T. Schmedt, M. M. Silva, A. Ziaei, U. Jurkunas, Molecular bases of corneal endothelial dystrophies. *Exp. Eye Res.* **95**, 24–34 (2012).
4. U. V. Jurkunas, Fuchs endothelial corneal dystrophy through the prism of oxidative stress. *Cornea* **37** (suppl. 1), S50–S54 (2018).
5. J. J. Doutch, A. J. Quantock, N. C. Joyce, K. M. Meek, Ultraviolet light transmission through the human corneal stroma is reduced in the periphery. *Biophys. J.* **102**, 1258–1264 (2012).
6. C. Zinflou, P. J. Rochette, Ultraviolet A-induced oxidation in cornea: Characterization of the early oxidation-related events. *Free Radic. Biol. Med.* **108**, 118–128 (2017).
7. A. J. Ridley, J. R. Whiteside, T. J. McMillan, S. L. Allinson, Cellular and sub-cellular responses to UVA in relation to carcinogenesis. *Int. J. Radiat. Biol.* **85**, 177–195 (2009).
8. G. F. Vile, R. M. Tyrrell, UVA radiation-induced oxidative damage to lipids and proteins in vitro and in human skin fibroblasts is dependent on iron and singlet oxygen. *Free Radic. Biol. Med.* **18**, 721–730 (1995).
9. N. C. Joyce, D. L. Harris, C. C. Zhu, Age-related gene response of human corneal endothelium to oxidative stress and DNA damage. *Invest. Ophthalmol. Vis. Sci.* **52**, 1641–1649 (2011).
10. A. Halilovic *et al.*, Menadione-induced DNA damage leads to mitochondrial dysfunction and fragmentation during rosette formation in fuchs endothelial corneal dystrophy. *Antioxid. Redox Signal.* **24**, 1072–1083 (2016).
11. P. Yeh, K. Colby, "Corneal endothelial dystrophies" in *The Cornea*, C. A. D. Foster, C. Dohlman, Eds. (Lippincott Williams & Wilkins, Philadelphia, 2004).
12. S. E. Wilson, W. M. Bourne, Fuchs' dystrophy. *Cornea* **7**, 2–18 (1988).
13. G. M. Zoega *et al.*, Prevalence and risk factors for cornea guttata in the Reykjavik Eye Study. *Ophthalmology* **113**, 565–569 (2006).
14. M. J. Hogan, I. Wood, M. Fine, Fuchs' endothelial dystrophy of the cornea. 29th Sanford Gifford Memorial lecture. *Am. J. Ophthalmol.* **78**, 363–383 (1974).
15. X. Zhang *et al.*; Fuchs' Genetics Multi-Center Study Group, Association of smoking and other risk factors with Fuchs' endothelial corneal dystrophy severity and corneal thickness. *Invest. Ophthalmol. Vis. Sci.* **54**, 5829–5835 (2013).
16. A. P. Adamis, V. Filatov, B. J. Tripathi, R. C. Tripathi, Fuchs' endothelial dystrophy of the cornea. *Surv. Ophthalmol.* **38**, 149–168 (1993).
17. E. Cavalieri *et al.*, Catechol estrogen quinones as initiators of breast and other human cancers: Implications for biomarkers of susceptibility and cancer prevention. *Biochim. Biophys. Acta* **1766**, 63–78 (2006).
18. E. L. Cavalieri, E. G. Rogan, Unbalanced metabolism of endogenous estrogens in the etiology and prevention of human cancer. *J. Steroid Biochem. Mol. Biol.* **125**, 169–180 (2011).
19. J. Hakkola *et al.*, Expression of CYP1B1 in human adult and fetal tissues and differential inducibility of CYP1B1 and CYP1A1 by Ah receptor ligands in human placenta and cultured cells. *Carcinogenesis* **18**, 391–397 (1997).
20. P. Pelkonen, M. Lang, M. Pasanen, Tissue and sex-dependent differences in CYP2A activities in hamsters. *Arch. Toxicol.* **68**, 416–422 (1994).
21. A. S. Jun *et al.*, An alpha 2 collagen VIII transgenic knock-in mouse model of Fuchs endothelial corneal dystrophy shows early endothelial cell unfolded protein response and apoptosis. *Hum. Mol. Genet.* **21**, 384–393 (2012).
22. U. V. Jurkunas, M. S. Bitar, T. Funaki, B. Azizi, Evidence of oxidative stress in the pathogenesis of fuchs endothelial corneal dystrophy. *Am. J. Pathol.* **177**, 2278–2289 (2010).
23. S. Y. Sun, N-acetylcysteine, reactive oxygen species and beyond. *Cancer Biol. Ther.* **9**, 109–110 (2010).
24. J. H. Santos, B. S. Mandavilli, B. Van Houten, Measuring oxidative mtDNA damage and repair using quantitative PCR. *Methods Mol. Biol.* **197**, 159–176 (2002).
25. N. K. Sharma *et al.*, Intrinsic mitochondrial DNA repair defects in Ataxia Telangiectasia. *DNA Repair (Amst.)* **13**, 22–31 (2014).
26. A. S. Benischke *et al.*, Activation of mitophagy leads to decline in Mfn2 and loss of mitochondrial mass in Fuchs endothelial corneal dystrophy. *Sci. Rep.* **7**, 6656 (2017).
27. T. Miyai *et al.*, Activation of PINK1-parkin-mediated mitophagy degrades mitochondrial quality control proteins in fuchs endothelial corneal dystrophy. *Am. J. Pathol.* **189**, 2061–2076 (2019).
28. H. Meng *et al.*, L450W and Q455K Col8a2 knock-in mouse models of Fuchs endothelial corneal dystrophy show distinct phenotypes and evidence for altered autophagy. *Invest. Ophthalmol. Vis. Sci.* **54**, 1887–1897 (2013).
29. M. C. Sangar, S. Bansal, N. G. Avadhani, Bimodal targeting of microsomal cytochrome P450s to mitochondria: Implications in drug metabolism and toxicity. *Expert Opin. Drug Metab. Toxicol.* **6**, 1231–1251 (2010).
30. E. L. Cavalieri, E. G. Rogan, M. Zahid, Critical depurinating DNA adducts: Estrogen adducts in the etiology and prevention of cancer and dopamine adducts in the etiology and prevention of Parkinson's disease. *Int. J. Cancer* **141**, 1078–1090 (2017).
31. J. T. Buters *et al.*, Cytochrome P450 CYP1B1 determines susceptibility to 7, 12-dimethylbenz[a]anthracene-induced lymphomas. *Proc. Natl. Acad. Sci. U.S.A.* **96**, 1977–1982 (1999).
32. K. H. Baratz *et al.*, E2-2 protein and Fuchs's corneal dystrophy. *N. Engl. J. Med.* **363**, 1016–1024 (2010).
33. N. A. Afshari *et al.*, Genome-wide association study identifies three novel loci in Fuchs endothelial corneal dystrophy. *Nat. Commun.* **8**, 14898 (2017).
34. S. A. Riazuddin *et al.*, Mutations in LOXHD1, a recessive-deafness locus, cause dominant late-onset Fuchs corneal dystrophy. *Am. J. Hum. Genet.* **90**, 533–539 (2012).
35. D. W. Chung, R. F. Frausto, L. B. Ann, M. S. Jang, A. J. Aldave, Functional impact of ZEB1 mutations associated with posterior polymorphous and Fuchs' endothelial corneal dystrophies. *Invest. Ophthalmol. Vis. Sci.* **55**, 6159–6166 (2014).
36. S. Biswas *et al.*, Missense mutations in COL8A2, the gene encoding the alpha2 chain of type VIII collagen, cause two forms of corneal endothelial dystrophy. *Hum. Mol. Genet.* **10**, 2415–2423 (2001).
37. M. Matthaei *et al.*, Fuchs endothelial corneal dystrophy: Clinical, genetic, pathophysiologic, and therapeutic aspects. *Annu. Rev. Vis. Sci.* **5**, 151–175 (2019).
38. J. D. Gottsch *et al.*, Inheritance of a novel COL8A2 mutation defines a distinct early-onset subtype of fuchs corneal dystrophy. *Invest. Ophthalmol. Vis. Sci.* **46**, 1934–1939 (2005).
39. E. D. Wieben *et al.*, A common trinucleotide repeat expansion within the transcription factor 4 (TCF4, E2-2) gene predicts Fuchs corneal dystrophy. *PLoS One* **7**, e49083 (2012).
40. J. Zhang, C. N. J. McGhee, D. V. Patel, The molecular basis of fuchs' endothelial corneal dystrophy. *Mol. Diagn. Ther.* **23**, 97–112 (2019).
41. U. V. Jurkunas *et al.*, Decreased expression of peroxiredoxins in Fuchs' endothelial dystrophy. *Invest. Ophthalmol. Vis. Sci.* **49**, 2956–2963 (2008).
42. C. Liu, D. Vojnovic, I. E. Kochevar, U. V. Jurkunas, UV-A irradiation activates Nrf2-regulated antioxidant defense and induces p53/caspase3-dependent apoptosis in corneal endothelial cells. *Invest. Ophthalmol. Vis. Sci.* **57**, 2319–2327 (2016).
43. G. Wollensak, E. Spoerl, M. Wilsch, T. Seiler, Endothelial cell damage after riboflavin-ultraviolet-A treatment in the rabbit. *J. Cataract Refract. Surg.* **29**, 1786–1790 (2003).
44. G. Wollensak, E. Spörl, F. Reber, L. Pillunat, R. Funk, Corneal endothelial cytotoxicity of riboflavin/UVA treatment in vitro. *Ophthalmic Res.* **35**, 324–328 (2003).
45. A. P. Cullen, Photokeratitis and other phototoxic effects on the cornea and conjunctiva. *Int. J. Toxicol.* **21**, 455–464 (2002).
46. A. R. Young, Acute effects of UVR on human eyes and skin. *Prog. Biophys. Mol. Biol.* **92**, 80–85 (2006).
47. J. P. Bergmanson, Corneal damage in photokeratitis–Why is it so painful? *Optom. Vis. Sci.* **67**, 407–413 (1990).
48. L. Behrendt, M. E. Jönsson, J. V. Goldstone, J. J. Stegeman, Induction of cytochrome P450 1 genes and stress response genes in developing zebrafish exposed to ultraviolet radiation. *Aquat. Toxicol.* **98**, 74–82 (2010).

49. G. Goerz *et al*., Influence of UVA and UVB irradiation on hepatic and cutaneous P450 isoenzymes. *Arch. Dermatol. Res.* **289**, 46–51 (1996).
50. R. K. Sindhu, F. E. Wagner, Y. Kikkawa, Induction of cytochrome p450 1A1 and 1B1 by photooxidized tryptophan in transformed human keratinocytes. *Adv. Exp. Med. Biol.* **527**, 297–306 (2003).
51. V. Vasiliou, F. J. Gonzalez, Role of CYP1B1 in glaucoma. *Annu. Rev. Pharmacol. Toxicol.* **48**, 333–358 (2008).
52. S. Bansal *et al*., Mitochondrial targeting of cytochrome P450 (CYP) 1B1 and its role in polycyclic aromatic hydrocarbon-induced mitochondrial dysfunction. *J. Biol. Chem.* **289**, 9936–9951 (2014).
53. F. M. Yakes, B. Van Houten, Mitochondrial DNA damage is more extensive and persists longer than nuclear DNA damage in human cells following oxidative stress. *Proc. Natl. Acad. Sci. U.S.A.* **94**, 514–519 (1997).
54. R. D. Thomas, D. Roy, Stilbene estrogen produces higher levels of mitochondrial DNA adducts than nuclear DNA adducts in the target organ of cancer (liver) of male Sprague Dawley rats. *Oncol. Rep.* **8**, 1035–1038 (2001).
55. R. D. Thomas, D. Roy, Base sequence-specific attack of stilbene estrogen metabolite(s) on the mitochondrial DNA: Implications in the induction of instability in the mitochondrial genome in the kidney of Syrian hamsters. *Int. J. Mol. Med.* **7**, 389–395 (2001).
56. J. D. Gottsch *et al*., Serial analysis of gene expression in the corneal endothelium of Fuchs' dystrophy. *Invest. Ophthalmol. Vis. Sci.* **44**, 594–599 (2003).
57. E. L. Cavalieri *et al*., Molecular origin of cancer: Catechol estrogen-3,4-quinones as endogenous tumor initiators. *Proc. Natl. Acad. Sci. U.S.A.* **94**, 10937–10942 (1997).
58. N. W. Gaikwad *et al*., Imbalanced estrogen metabolism in the brain: Possible relevance to the etiology of Parkinson's disease. *Biomarkers* **16**, 434–444 (2011).
59. S. Pruthi *et al*., Evaluation of serum estrogen-DNA adducts as potential biomarkers for breast cancer risk. *J. Steroid Biochem. Mol. Biol.* **132**, 73–79 (2012).
60. M. Zahid *et al*., Unbalanced estrogen metabolism in ovarian cancer. *Int. J. Cancer* **134**, 2414–2423 (2014).
61. S. L. Byers, M. V. Wiles, S. L. Dunn, R. A. Taft, Mouse estrous cycle identification tool and images. *PLoS One* **7**, e35538 (2012).
62. T. Schmedt *et al*., Telomerase immortalization of human corneal endothelial cells yields functional hexagonal monolayers. *PLoS One* **7**, e51427 (2012).
63. B. Mondal *et al*., Modulation of cellular response to arsenic trioxide toxicity by resveratrol. *ACS Omega* **3**, 5511–5515 (2018).